Surface Science 666 (2017) 28–43

Contents lists available at ScienceDirect

Surface Science

journal homepage: www.elsevier.com/locate/susc

Oxygen adsorption at heterophase boundaries of the oxygenated Cu(110)

Dongxiang Wu [a], Jonathan Li [b], Guangwen Zhou [a,*]

[a] Department of Mechanical Engineering & Materials Science and Engineering Program, State University of New York, Binghamton, NY 13902, USA
[b] Department of Physics, Applied Physics and Astronomy & Materials Science and Engineering Program, State University of New York, Binghamton, NY 13902, USA

A B S T R A C T

Many metal-oxygen systems involve progressive stages of oxygen chemisorption induced surface phase transition and restructuring that result in the formation of heterophase boundaries within the oxygen chemisorbed layer. Using the density functional theory calculations, we investigated the effect of such heterophase boundaries formed by the (2×1)-O → c(6×2)-O phase transition on Cu(110) on the onset of bulk oxidation. Upon the increased oxygen coverage, we show that some (2×1)/(6×2) boundaries allow for further propagation of the (2×1)/(6×2) phase boundary while the other boundaries promote subsurface oxygen adsorption that results in the formation of Cu_2O-like tetrahedrons. By comparing the surface height of the Cu atoms within the heterophase boundary area, we show that the boundaries with a larger surface elevation of the Cu atoms are prone to form Cu_2O-like tetrahedrons by subsurface oxygen occupancy. These results indicate that the presence of the two-phase boundaries formed by the surface phase transition in the oxygen chemisorbed layer facilitates the inward diffusion of oxygen atoms and thus initiates the onset of bulk oxidation.

1. Introduction

The exposure of a metallic surface to gaseous oxygen usually results in the oxidation of the metal. Such a gas-surface reaction plays a crucial role in many technological processes including chemical catalysis, corrosion, high-temperature oxidation and solar conversion [1–4]. The typical pathway of the surface oxidation proceeds from the initial stages of oxygen chemisorption induced surface restructuring and oxygen subsurface adsorption to oxide nucleation and growth and then to the oxide thickening [5–7]. While the understanding of oxygen chemisorption induced surface structuring and the later stages of oxide thickening has been relatively well established, the microscopic process governing the transition from a two-dimensional (2D) oxygen chemisorbed layer to the nucleation and growth of a 3D oxide phase is still significantly unclear, due largely to the experimental difficulties in resolving these atomic processes occurring in both the surface and subsurface regions. The nucleation of a bulk oxide phase requires the incorporation of oxygen through the oxygen chemisorbed layer into the subsurface region. An information gap still exists regarding the atomic detail of the transformation of a metal lattice into the oxide lattice upon oxygen subsurface adsorption. King and co-workers proposed that a critical oxygen coverage is required at which the oxygen atoms spontaneously embed themselves into the subsurface region, initializing the oxide formation [8–10]. The oxygen subsurface occupation is due to the strong repulsive force between oxygen atoms in the chemisorbed layer that results in dramatic drop of the heat of adsorption with increasing oxygen coverage. While this model illustrates why a critical oxygen coverage is needed for spontaneous oxide formation, it does not explain the microscopic pathway of the crossover from the 2D chemisorbed layer to 3D oxide formation and does not account for the effect of structural defects in the oxygen chemisorbed layer on oxygen subsurface embedment for oxide formation. Generally, there is a lack of systematic study of the effect of structural defects in an oxygen chemisorbed layer on-surface O adsorption and subsequent oxide formation enabled by subsurface oxygen uptake.

Like most transition metals, the Cu-O system has received extensive interest for its technological importance such as Cu-based catalysts [11–13]. Particularly, Cu(110) is the most open of the well-studied low-index surfaces of oxygen adsorption and the related surface restructuring processes [14–23]. It has been well established that the oxygen adsorption on Cu(110) first results in an added-row (2×1) reconstruction [17,18,24,25] that transits to the (6×2) reconstruction upon further oxygen adsorption [14,15,17]. With a suitable oxygen chemical potential bias, the Cu_2O phase is expected to set in after the (6×2) reconstruction [20,26]. The formation of the bulk oxide phase (e.g., Cu_2O) for a planar surface requires the embedment of oxygen atoms through the oxygen chemisorption reconstructed layer into the subsurface region. In FCC (face-centered cubic) Cu lattice, there are two types of interstitial sites, i.e., octahedral and tetrahedral sites, available for possible subsurface oxygen occupancy. It has been shown that the octahedral sites are energetically more favored than the tetrahedral sites for the initial subsurface oxygen adsorption [27–32]. In the Cu_2O lattice, oxygen has to reside at the tetrahedral sites of FCC Cu lattice. Therefore, the crossover from the oxygen octahedral occupancy to the tetrahedral occupancy represents a crucial step in the onset of bulk oxidation.

Scanning tunneling microscopy (STM) studies have shown that the Cu(110)-(6×2) reconstruction occurs via the nucleation and growth of (6×2) domains out of the (2×1) reconstructed layer [26,33–35]. This

* Corresponding author.
E-mail address: gzhou@binghamton.edu (G. Zhou).

http://dx.doi.org/10.1016/j.susc.2017.08.017
Received 5 April 2017; Received in revised form 19 August 2017; Accepted 22 August 2017
Available online 24 August 2017
0039-6028/

surface phase transition process results in the formation of a large number of domain boundaries between the (2×1) and (6×2) phases. The goal of this study is to employ density-functional theory (DFT) to investigate the effect of merged (2×1)/(6×2) boundaries on subsurface oxygen adsorption. While structural defects such as step edges are usually regarded as preferential sites for oxide nucleation [26,34,36,37], the presence of structure defects such as the domain or heterophase boundaries in a chemisorbed layer and their effect on subsurface oxygen adsorption induced bulk oxidation still remain largely uninvestigated. Although the boundary structures (and even subsurface oxygen) may be resolved experimentally such as by STM imaging, dynamically probing the microscopic processes leading to the crossover from the 2D chemisorbed layer to a 3D oxide still represents a challenge. DFT is a powerful tool to bridge this gap by providing the atomistic mechanism of the oxygen adsorption induced structural evolution in both surface and subsurface regions. We previously reported the DFT study of oxygen adsorption at homophase boundaries formed by the merging of domains of the same chemisorbed phase, *i.e.*, the boundaries formed by mismatched missing rows of the oxygen-chemisorbed $(2\sqrt{2}\times\sqrt{2})R45°$-O domains on Cu(100) and the boundaries by mismatched Cu-O–Cu rows of the oxygen-chemisorbed (2×1)-O domains on Cu(110), and the DFT results showed that these boundaries are the preferred sites for oxygen subsurface adsorption, thereby facilitating the bulk oxide formation in the subsurface region [27,38]. In this work, we extend the study to the heterophase boundaries formed from the (2×1)→(6×2) phase transition. Our results show that some (2×1)/(6×2) boundaries allow for further on-surface oxygen adsorption thereby resulting in the (2×1)→(6×2) phase transition while the other (2×1)/(6×2) boundaries facilitate subsurface oxygen adsorption that induces the onset of bulk oxidation even in the early stage of the oxygen chemisorption induced surface restructuring process.

2. Computational methods

Periodic DFT calculations were performed using the Vienna Ab initio Simulation Package (VASP) [39–42]. PW91 generalized gradient approximation (GGA) [43] was used to describe the electron–electron exchange and correlation interactions. We used the projector augmented-wave (PAW) potential [44] to modeled core-electron potential. To test the cut-off energy, we used the energy of 380 eV and 450 eV to perform an adsorption energy test, and we found that the value of 380 eV is sufficient since the difference between the two tested energies is less than 0.01 eV, which agrees with the previous study [38,45]. The Brillouin-zone integration was performed using (2×4×1) K-point meshes based on Monkhorst–Pack grids [46]. We also carried out a convergence test of the K-points mesh by comparing the total energy difference of the slab containing (2×1)/(6×2) domain boundaries using (2×4×1) and (4×8×1) meshes, which indicates that the (4×8×1) mesh gives a total energy difference of less than 0.02 eV, suggesting that sufficient convergence is reached using the (2×4×1) mesh. We used period slabs with a vacuum spacing 12 Å to model the Cu (110) surface, and the slab is composed of 5 layers with the bottom two layers fixed, while the other three top layers are free to relax until all force components acting on the atoms are below 0.015 eV/Å. We calculated the lattice parameter of Cu to be 3.64 Å, which is in good agreement with previous calculations [20,24,28,38] and the experimental value of 3.61 Å [47]. We used the nudged elastic bands (NEB) method to calculate the reaction barrier and diffusion pathway [48], with five intermediate images between the initial state to the final state.

We investigated the oxygen adsorption energies and structure evolution by sequentially adsorbing a single oxygen atom for each calculation. The most stable configuration identified after adsorbing an oxygen atom was used as the reference state for the next oxygen atom to be adsorbed. The oxygen adsorption energy E_{ads} was calculated using the equation

$$E_{ads}=\frac{1}{N_O}\left(E^{tot}_{O/Cu}-E_{ref}-\frac{No}{2}E_{O_2}\right), \quad (1)$$

where No is the number of oxygen atoms newly adsorbed into the system, which is equal to 1 throughout the whole work for sequentially increasing the oxygen coverage by a single oxygen atom; $E^{tot}_{O/Cu}$ is the total energy of the whole Cu-O system; E_{ref} is the energy of the reference state, i.e., the energy of the most stable configuration with one fewer adsorbed oxygen atom compared with the system under study; E_{O_2} is energy of an isolated oxygen molecule.

Considering the relative stability of the different (2×1)/(6×2) boundaries, we also calculated the boundary formation energy ΔE by the following equation

$$\Delta E=\frac{1}{S}\left(E_{tot}-E_p-N_{atom}E_{atom}\right), \quad (2)$$

where E_{tot} is total energy of the system with a (2×1)/(6×2) boundary; *Ep* is the total energy of the reference slab of either the perfect (2×1)-O or (6×2)-O surface (i.e., both the perfect (2×1)-O or (6×2)-O surfaces are used as the reference slab to evaluate the boundary formation energy because the boundary formation involves merging (2×1)-O and (6×2)-O domains); N_{atom} is the number of Cu or O atoms added to the system with the (2×1)/(6×2) boundaries; and E_{atom} is the energy of either a Cu atom in the bulk (calculated by dividing the total energy of Cu atoms in a bulk system by the number of Cu atoms in the cell) or a single O atom (half of the total energy of an isolated O_2 molecule), and S is the surface area of the system. The atomic structures are visualized using the Visualization for Electronic and Structure Analysis (VESTA).

3. Results and discussion

Upon oxygen exposure, Cu(110) first develops into a well ordered (2×1) reconstruction with an oxygen coverage $\theta = 0.5$. This O-chemisorbed phase is composed of Cu-O–Cu chains aligned along the [001] direction of the Cu(110) substrate in every other [110]-(1×1) spacing, where the O atoms reside at the long bridge sites between Cu atoms (Fig. 1(a)). Further oxygen exposure results in the nucleation and growth of the (6×2) reconstruction with a saturated oxygen coverage $\theta = 0.67$, which consists of two [001] oriented Cu-O–Cu chains in every three [110]-(1×1) lattice spacings and alternative Cu atoms and vacancies on every third [001] rows (Fig. 1(b)). Heterophase boundaries form by the nucleation and growth of (6×2) domains in the existing (2×1) chemisorbed layer. Although the stochastic nature of the nucleation process results in the random distribution of (6×2) domains within the (2×1) chemisorbed layer with the formation of a high density of (6×2)/(2×1) boundaries, the two-phase boundaries can only be along the [100] or [1$\bar{1}$0] direction of the substrate because of the two-fold symmetry of the Cu(110) surface.

By considering all the scenarios of the geometric alignment of (6×2) and (2×1) domains, a total of ten different heterophase boundary structures can develop between the two structures, depending on the orientations of the boundaries. For boundaries parallel to the [1$\bar{1}$0] direction of the substrate, four types of the boundaries, denoted as [1$\bar{1}$0]-I, -II, -III, and –IV, can develop (Fig. 2(a–d)). [1$\bar{1}$0]-I is formed by combining row R2 of the (2×1) with R1 of the (6×2) and aligning L1-L7 in the two cells, where columns L1-L2 and rows R1-R2 in the (2×1) structure are defined in Fig. 1(a), and columns L1-L7 and rows R1-R5 are given in Fig. 1(b). Noticing that the two atoms at the boundary marked as green balls in the [1$\bar{1}$0]-I boundary (Fig. 2(a)) can be either O related to the (2×1) structure or Cu related to the (6×2) structure. However, the placement of Cu atoms at these two sites results in their close proximity with the Cu atoms in the adjacent Cu column (i.e., R1 shown in Fig. 1(a)) of the (2×1) region and our DFT calculations show that such a configuration is highly unstable. Instead, the placement of O atoms at the two sites stabilizes the boundary, which results in an O-only boundary (Fig. 2(a)). Fig. 2(b) shows the [1$\bar{1}$0]-II boundary formed by combining atom row R2 of the (2×1) with R1 of the (6×2) but with the misalignment of the (6×2) and (2×1) cells by a half unit cell distance along the [1$\bar{1}$0] direction. Fig. 2(c and d) show the [1$\bar{1}$0]-III and [1$\bar{1}$0]-VI boundaries formed by combining row R1 of the (2×1) with R2 of

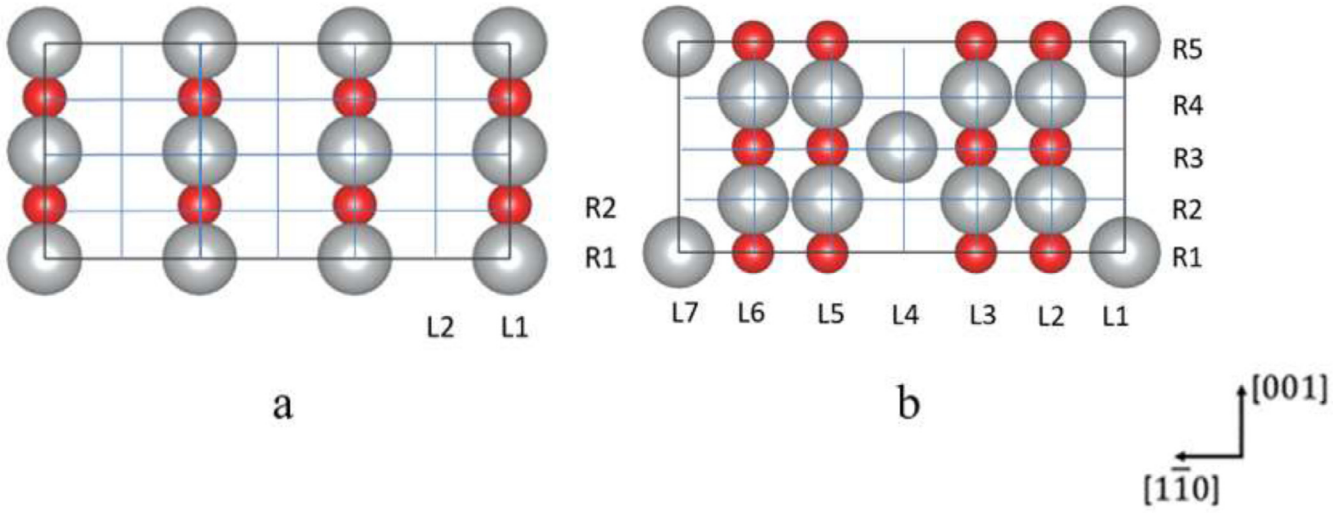

Fig. 1. The atomic structural models of (a) the perfect (2×1) reconstruction, (b) the perfect (6×2) reconstruction. Grey and red balls represent Cu and O atoms, respectively. (For interpretation of the references to colour in this figure legend, the reader is referred to the web version of this article.)

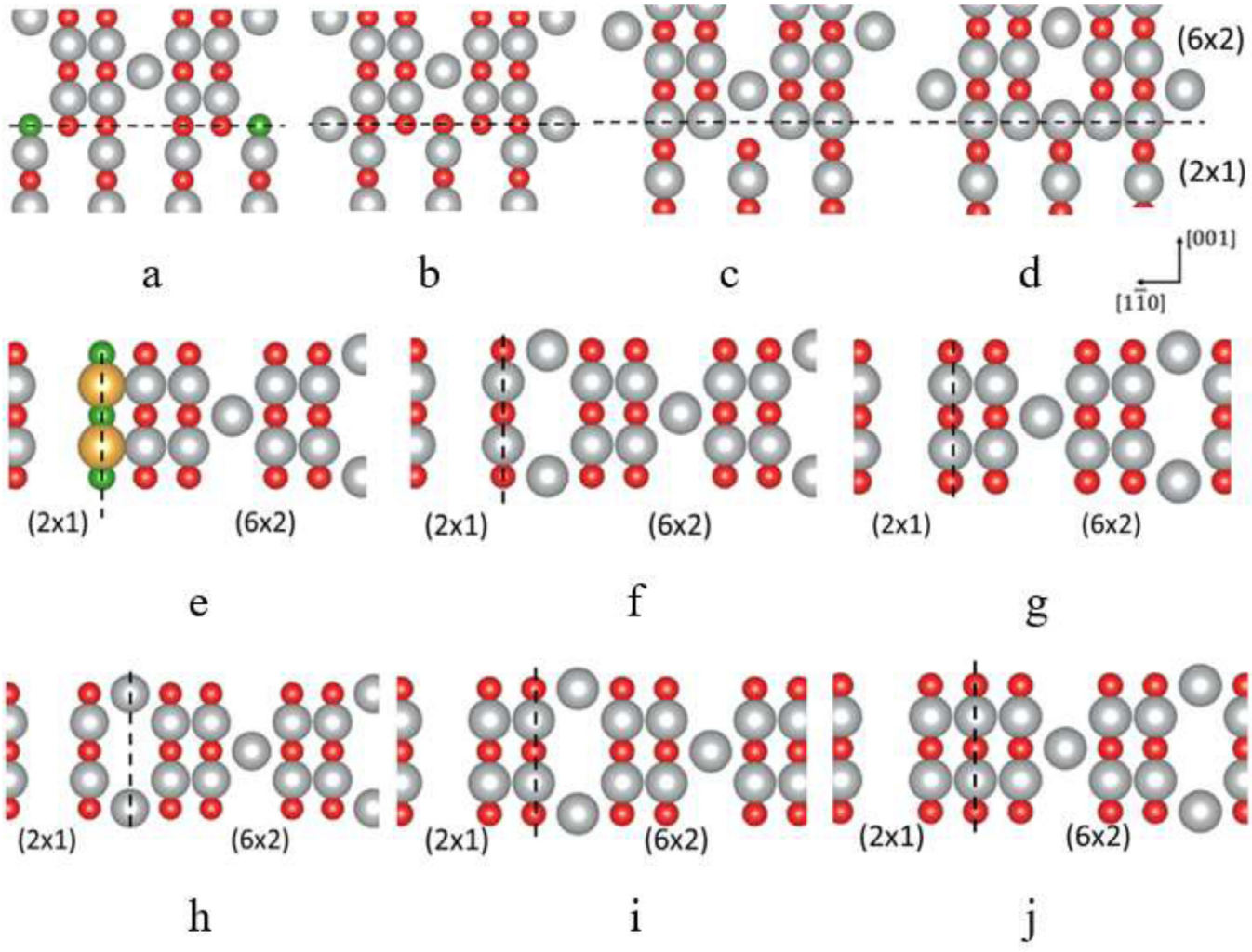

Fig. 2. Structural models of all the possible boundaries formed between (2×1) and (6×2) domains. (a)–(d) all the [1$\bar{1}$0] types, formed by combing the column of (2×1) and (6×2); (e)–(j) all the [100] types domain boundary, formed by combine the row of (2×1) and (6×2). All the grey balls represent the surface copper atoms, and oxygen atoms are depicted by red balls. The green balls in (a) represent oxygen atoms that replace the original copper atoms, while the gold and green balls in (e) represent copper atoms and oxygen atoms, which means the Cu-O–Cu chain in (2×1) reconstruction replaces the isolated copper atoms in (6×2). The dotted line represents domain boundary formed by (2×1) and (6×2) recosntruction. (For interpretation of the references to colour in this figure legend, the reader is referred to the web version of this article.)

Table 1
Formation energies (eV) of (2×1)/(6×2) heterophase boundaries with respect to the perfect (2×1)-O and (6×2)-O reconstructions.

	With respect to the (2×1)-O	With respect to the (6×2)-O
[1$\bar{1}$0]-I	−0.0219	0.0146
[1$\bar{1}$0]-II	−0.0249	0.0085
[1$\bar{1}$0]-III	−0.0134	0.0205
[1$\bar{1}$0]-IV	−0.0134	0.0205
[100]-I	−0.0289	0.00167
[100]-II	−0.0198	0.0107
[100]-III	−0.0198	0.0107
[100]-IV	−0.0192	0.0113
[100]-V	−0.0298	0.00143
[100]-VI	−0.0298	0.00143

the (6×2), and row R1 of the (2×1) with R4 of the (6×2) with column L1-L7 aligned, respectively. Noticing that the hall-unit cell shift along the [1$\bar{1}$0] direction of the [1$\bar{1}$0]-III or [1$\bar{1}$0]-VI boundaries does not lead to any new configurations. Other combinations of the rows and columns shown in Fig. 1(a, b) are either redundant or restricted by the atom arrangement of the Cu substrate. Along the [100] direction of the Cu substrate, six different (6×2)/(2×1) boundaries can develop similarly, i.e., [100]-I, -II, -III, –IV, -V and -VI, as shown in Fig. 2(g–j). It is worth mentioning that the [100]-I boundary (Fig. 2(e)) can be either a Cu-O–Cu chain of the (2×1) structure (i.e., column L1 type, as shown in Fig. 1(a)) or two isolated Cu atoms of the (6×2) structure (i.e., column L1 type, shown in Fig. 1(b)). Our DFT calculations show that the configuration with the Cu-O–Cu chain being the boundary is much more stable than placing two isolated Cu atoms at the boundary. Therefore, the configuration with the Cu-O–Cu chain being the boundary (Fig. 2(e)) is adopted in our calculations. To compare the relative stability of the different boundaries constructed above, the formation energies of all the boundaries are calculated using Eq. (2). As shown in Table 1, the formation energies for all the boundaries are negative with respect to the (2×1) reconstruction, whereas slightly positive, less than 0.03 eV, with respect to the (6×2) reconstruction, implying that the heterophase boundaries have a trend to transform to the (6×2) structure. However, these boundaries can still exist because they are formed from the randomly nucleated (6×2) domains within the (2×1) layer. Although these boundaries are not equally stable, transformation from one boundary to the other type can be kinetically hindered because such transformation requires massive structure changes involved. Therefore, once a boundary is formed, it persists even it is thermodynamically unfavorable. This is in a good analogy to the presence of grain boundaries in materials although they are high-energy defects and thermodynamically unfavorable.

It is worth mentioning that the surface coverage of Cu and O for the (2×1)-O reconstruction is $\theta = 0.5$ ML and this corresponds to an atomic surface density of 0.05/Å^2. For the c(6×2)-O reconstruction, the surface coverages of Cu and O are $\theta = 5/6$ and 2/3, respectively, which can be translated to the atomic surface densities of 0.09/Å^2 and 0.07/Å^2. Therefore, the formation of the various (2×1)/(6×2) boundaries requires incorporation of new Cu and O atoms from the surrounding area, where O atoms are supplied from the adsorbed oxygen for increased oxygen exposure, while Cu atoms can be supplied from the immediate sources of terraces or step edges, as shown from STM experiments [24,26].

Different supercells are constructed for the different heterophase boundaries and all the supercells with two boundaries are constructed for maintaining the 2D periodicity in the cell geometry. Boundaries [1$\bar{1}$0]-III and -IV are combined in the same supercell (Figs. 5 and 6). Similarly, boundaries [100]-II and [100]-III are incorporated into one supercell (Figs. 8 and 9), and boundaries [100]-V and [100]-VI are combined into another supercell (Figs. 11 and 12). It is crucial to include sufficient space between the two boundaries in the supercells to eliminate any appreciable boundary-boundary interactions. The supercell sizes are 25.48 Å and 15.44 Å for [1$\bar{1}$0]-type domain boundaries and 7.28 Å and 46.33 Å for [100]-type domain boundaries. We compare the on-surface oxygen adsorption energies at a hollow site halfway between the boundaries for the different supercells with an equivalent hollow site of the perfect (2×1) cell. Their energy differences are less than 0.06 eV for all the supercells, indicating that the size of our constructed supercells is sufficient so that any boundary-boundary interaction has negligible effect for the cells. We can also check the oxygen adsorption energy with smaller supercell cells (i.e., 15.2 Å×15.44 Å for [1$\bar{1}$0]-type boundaries and 7.28 Å×30.89 Å for the [100]-type boundaries), which result in larger differences, 0.54 eV and 0.63 eV, compared with the perfect (2×1) cell.

We examine both on-surface and subsurface sites for O adsorption by calculating O adsorption energy for each on-surface and subsurface adsorption site in the boundary area. All the possible O adsorption sites within one atomic displacement in the [100] direction perpendicular to the [1$\bar{1}$0]-type boundaries and in the [1$\bar{1}$0] direction perpendicular to the [100]-type boundaries are identified and considered. The sites located more than one atomic displacement away from the heterophase boundaries have the similar O adsorption behavior of the perfect (2×1) or (6×2) structures and are thus not considered further. Within the one atomic displacement from the boundaries, there are five distinct on-surface O adsorption sites: the hollow site (H) located above the center of four surface Cu atoms, the long-bridge (lb) site between pairs of surface Cu atoms along the [110] direction, the short-bridge (sb) site along pairs of surface Cu atoms along the [001] direction, the open sites (op) along the open [001] Cu rows, and the shift-hollow (shH) site above half-way between the hollow and short-bridge sites. Finally, the top site is direct above a surface Cu atom and has been shown to be unstable [18,20,28,38], and not further explored except for our first calculation as a test. The possible subsurface O adsorption sites can be either the tetrahedral (T) site coordinated by four neighboring Cu atoms or the octahedral (O) site coordinated by six neighboring Cu atoms. We have performed calculations of oxygen adsorption at the oxygen coverages up to $\theta = 0.69$ (the coverage is defined by the ratio of the number of O atoms over the number of the Cu atoms in the corresponding clean surface) and subsurface sites located in the second outermost layer and have not considered the subsurface adsorption sites deeper in the third layer

3.1. [1$\bar{1}$0]-type boundaries

The supercell for the [1$\bar{1}$0]-I boundary is shown in Fig. 3(a), which contains 196 Cu atoms and 28 O atoms with the oxygen coverage $\theta = 0.67$. Because it is an O-only boundary, the on-surface lb sites do not exist. We comparatively examine O adsorption at the on-surface sites of sb, op, H, shH and the subsurface sites with the oxygen coverage $\theta = 0.69$. All the non-equivalent on-surface and subsurface sites are marked in Fig. 3(a and b), respectively. The calculated adsorption energies of all these on-surface and subsurface sites are listed in Table 2. The sb site has a positive value of the adsorption energy, indicating an endothermic and unfavorable adsorption process. Due to the O–O repulsion force, both of the O atoms at the on-surface H and shH sites diffuses further than one atomic displacement from the O-only boundary to the equivalent shH sites of either the perfect (2×1) or (6×2) region and stabilizes there. Although the O atom at the op site has less negative adsorption energy compared to the H and shH sites, it can stabilize there. While O6 and O2 yield the most negative binding energies for subsurface O adsorption, the O atoms placed at these two sites cannot stabilize there. Instead, they diffuse more than one atomic displacement away from the boundary to the on-surface shH sites of the (2×1) region and thus not explored further. The next most stable subsurface site is T1 with the O adsorption energy of −0.79 eV and the O atom placed at this site finally diffuses deeper and stays at the octahedral site between the second and third layers. O3 and T3 are the next favorable subsurface sites compared to the T1 site and O adsorption at these two sites results in

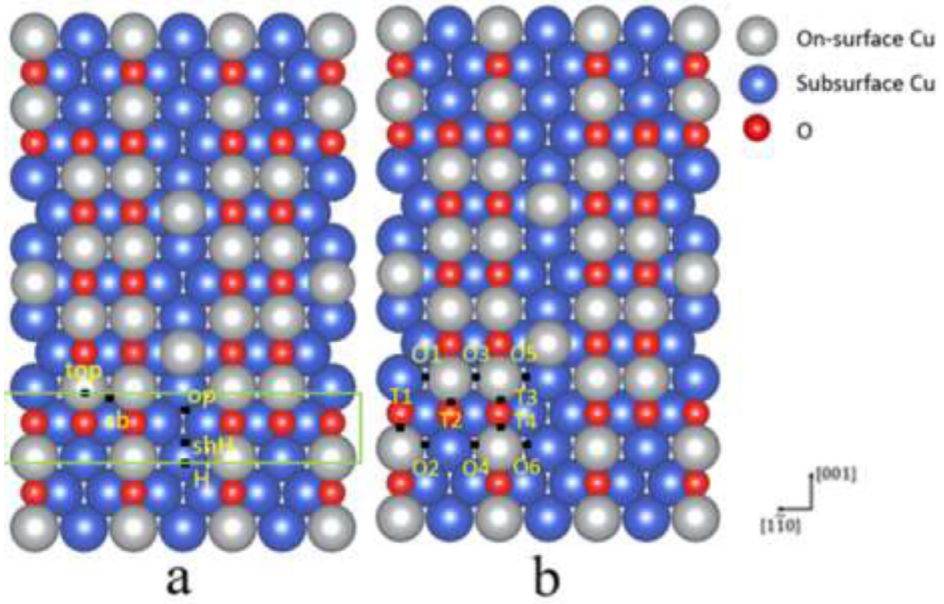

Fig. 3. [1$\bar{1}$0]-I boundary and the approximate locations of adsorption sites for possible oxygen occupancy. (a) on-surface sites, (b) subsurface sites. The green rectangle in (a) marks the oxygen adsorption area that is within one atomic displacement in the [100] direction perpendicular to the [1$\bar{1}$0] boundaries. (For interpretation of the references to colour in this figure legend, the reader is referred to the web version of this article.)

Table 2
Oxygen adsorption energies for all the possible sites along the [1$\bar{1}$0]-I boundary at the oxygen coverage $\theta = 0.67$.

Site	E_{ads}(eV)	Stabilized site
op	−0.46	
shH	−1.05	move away from the boundary
H	−1.05	move away from the boundary
sb	0.13	
O1	−0.54	
O2	−1.18	
O3	−0.66	O3 to T3
O4	−0.66	
O5	−0.44	
O6	−1.05	move away from the boundary
T1	−0.79	lower octahedral site
T2	0.12	
T3	−0.66	
T4	−0.66	T4 to O4

Table 3
Oxygen adsorption energies for all the possible sites along the [1$\bar{1}$0]-II boundary at the oxygen coverage $\theta = 0.67$.

Site	E_{ads}(eV)	Stabilized site
H	−1.59	Move away from the boundary
sb	−0.19	sb to O3
O1	−0.67	
O2	−0.68	
O3	−0.19	O3 to T3
O4	−1.03	
O5	−0.57	
O6	−1.56	Move away from the boundary
T1	−0.59	
T2	−0.50	
T3	−0.57	T3 to O5
T4	−0.72	Lower octahedral site

the same equilibrium configuration, stabilized at the same tetrahedral site (T3) in the second layer. These results shown above indicate that the [1$\bar{1}$0]-I boundary strongly favors the on-surface O occupation that facilitates the $(2\times1)\rightarrow(6\times2)$ phase transition if additional Cu atoms are available.

Fig. 4(a) shows the supercell for the [1$\bar{1}$0]-II boundary, which consists of 198 Cu atoms and 28 O atoms with the oxygen coverage $\theta = 0.67$. All the potential on-surface and subsurface sites are marked in Fig. 4(a and b), respectively. The adsorption of one additional O atom into the system reaches the total oxygen coverage $\theta = 0.69$. The calculated binding energies for the adsorption of one O atom at the different sites are listed in Table 3. Similar as the [1$\bar{1}$0]-I boundary, the [1$\bar{1}$0]-II boundary also contains a high density of O atoms in the boundary area. O atoms placed at both H and O6 sites are found to diffuse away from the boundary by one atomic displacement to the equivalent shH sits of the (2×1) regions and yield the most negative binding energies for O adsorption. O cannot stabilize at the sb site either and embeds into the subsurface octahedral O3 site. The next most stable site is the 5-fold octahedral site O4 with adsorption energy −1.04 eV. The most stable tetrahedron site is the T4 site, but the O atom cannot stabilize at the T4 site. Instead, it diffuses deeper and stays at the octahedral site between the second and third layers after optimizing. The next most stable tetrahedral site is T1 with adsorption energy −0.59 eV, and oxygen can stabilize at the second layer forming the Cu_2O-like tetrahedron. These results show that [1$\bar{1}$0]-II favors the on-surface O adsorption, similar to the O adsorption at the [1$\bar{1}$0]-I boundary shown above.

Unlike boundaries [1$\bar{1}$0]-I and -II, boundaries [1$\bar{1}$0]-III and -IV can be incorporated into a non-symmetry supercell (Figs. 5 and 6), and oxygen adsorption at one boundary does not affect the other boundary because our supercell is sufficiently large to eliminate any boundary–boundary interactions. All the possible sites for both on-surface and subsurface oxygen occupancy along the [1$\bar{1}$0]-III boundary are identified and shown in Fig. 5(a and b), respectively. The calculated binding energies for the adsorption of one O atom (with the oxygen coverage = 0.61) at the different sites are listed in Table 4. The most favorable site for oxygen adsorption is the lb site with an adsorption energy of −1.51 eV Oxygen adsorption at the other on-surface sites (shH and op sites) is less favorable but still has a negative binding energy. By contrast, all the subsurface sites are not stable for oxygen adsorption, and oxygen atoms placed at these sites diffuse to adjacent on-surface sites.

We then add another oxygen atom into the [1$\bar{1}$0]-III boundary of the most stable configuration with the oxygen occupancy at the lb site

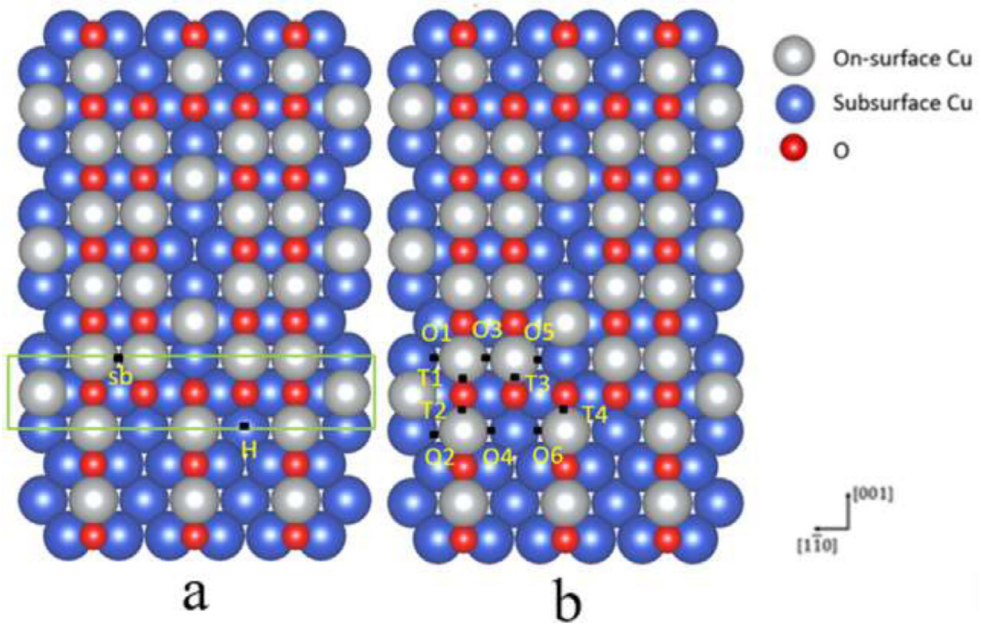

Fig. 4. [1$\bar{1}$0]-II boundary and the approximate locations of adsorption sites for possible (a) on-surface adsorption sites, (b) subsurface adsorption sites. The green rectangle marks the oxygen adsorption area which is within one atomic displacement in the [100] direction perpendicular to the [1$\bar{1}$0]-type boundaries. (For interpretation of the references to colour in this figure legend, the reader is referred to the web version of this article.)

Table 4
Oxygen adsorption energies for all the possible sites for the [1$\bar{1}$0]-III boundary at the oxygen coverage $\theta = 0.59$, 0.61, 0.64, and 0.67 respectively. The site sb1 at the oxygen coverage $\theta = 0.59$ is marked as sb in Fig. 4(a).

	$\theta = 0.59$		$\theta = 0.61$		$\theta = 0.64$		$\theta = 0.67$	
	E_{ads}(eV)	Stabilize site	E_{ads}(eV)	Stabilize site	E_{ads}(eV)	Stabilize site	E_{ads}(eV)	Stabilize site
lb	−1.51		−1.30					
sb1	−0.43		−0.73	O2	−0.25	O1	−0.26	O1
sb2			−1.15	O5	−0.55	O2		
H1	−1.32		−1.33	shH1				
H2	−1.51	lb	−1.30					
shH1	−1.05		−1.33					
shH2	−1.07		−1.33	shH1				
shH3	−1.29		−1.08					
op					−0.46		−0.52	
O1	−1.07	shH2	−1.33	shH1	−0.25		−0.26	
O2	−1.51	lb	−0.73		−0.35		−0.34	
O3	−1.51	lb	−0.37		−0.45		−0.47	
O4			−0.40		−0.55			
O5			−1.15					
O6			−1.34	shH1				
T1	−1.07	shH2	−0.73	O2	−0.25	O1	−0.26	O1
T2	−1.07	shH2	−0.73	O2	−0.25	O1	−0.26	
T3	−1.29	shH3	−0.69		−0.42		−0.26	O1
T4	−1.51	lb	−0.37	O3	−0.25	O1	0.017	
T5			−1.04		−0.50		−0.23	
T6			−1.30	lb	−0.55	O2	−0.33	
T7			−1.33	shH1	−0.55	O2	−0.56	
T8			−1.33	shH1	−0.55	O2	−0.73	

and achieve a higher oxygen coverage of $\theta = 0.64$. The various surface and subsurface sites for oxygen adsorption are shown in Fig. 5(c and d), respectively. Noticing that oxygen adsorption at the lb site lowers the symmetry of the system and thus significantly increases the number of nonequivalent subsurface sites for the adsorption of the second O atom. The adsorption energies for the nonequivalent positions are listed in Table 4. The on-surface shH1 site is the most stable adsorption position with the adsorption energy of −1.33 eV. It can be also noted that the increased oxygen coverage promotes the stability of the subsurface adsorption. The most favorable subsurface site is O5 with the oxygen adsorption energy of −1.15 eV. Although the tetrahedral sites are less favorable, some sites like T5 yield a negative oxygen binding energy as low as −1.04 eV. We then add the third O into the [1$\bar{1}$0]-III boundary with the oxygen occupancy at the lb and shH1 sites and reach the oxygen coverage $\theta = 0.67$. At this time, the on-surface sites do not yield the lowest system energy anymore; instead, the octahedral site O4 becomes the most stable site with the adsorption energy −0.55 eV. O placed initially at the sites of T6, T7, T8 and sb2 sites results in the similar adsorption energy −0.55 eV and stabilizes at O4 in the relaxed structure. We then continue to further adsorb the forth O atom at the [1$\bar{1}$0]-III boundary to reach the oxygen coverage $\theta = 0.69$ with the pre-adsorbed O at the on-surface lb and shH1 sites. The nonequivalent surface and subsurface sites for oxygen adsorption are marked in Fig. 5(g and h), respectively. At this high oxygen coverage, the most stable site is tetrahedral site T8,

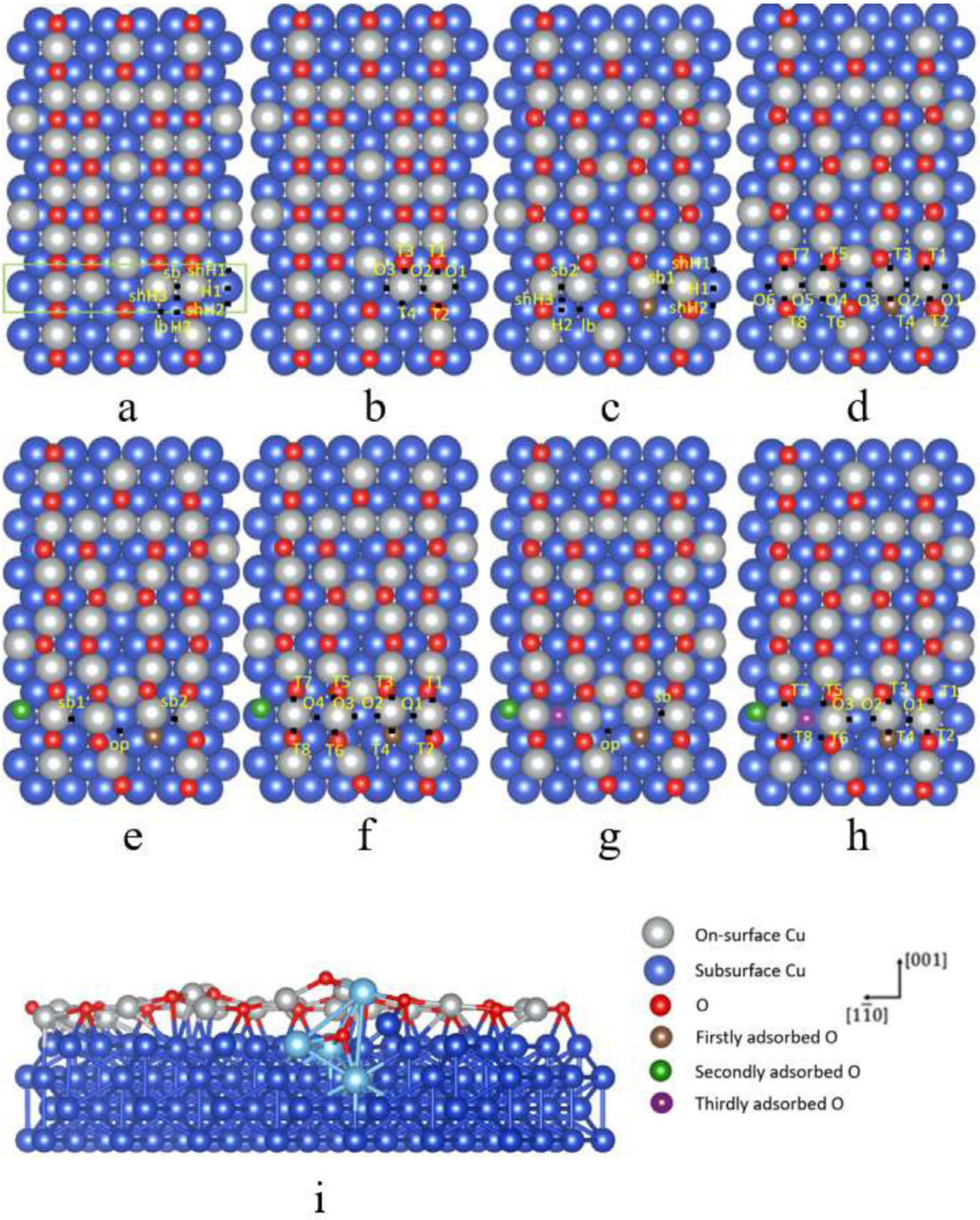

Fig. 5. [1$\bar{1}$0]-III boundary and the approximate locations of adsorption sites for possible (a) on-surface adsorption sites at coverage $\theta = 0.59$, (b) subsurface adsorption sites $\theta = 0.59$. (c) on-surface adsorption sites at coverage $\theta = 0.61$, (d) subsurface adsorption sites $\theta = 0.61$. (e) on-surface adsorption sites at coverage $\theta = 0.64$, (f) subsurface adsorption sites $\theta = 0.64$. (g) on-surface adsorption sites at coverage $\theta = 0.67$ (h) subsurface adsorption sites $\theta = 0.67$. (i) The equilibrium structure of the tetrahedron formed from the oxygen subsurface adsorption at T7 at the oxygen coverage $\theta = 0.69$ and the resulting Cu_2O-like tetrahedron is highlighted in blue. Similarly, the green rectangle represents the oxygen adsorption area at the [1$\bar{1}$0]-type boundaries. (For interpretation of the references to colour in this figure legend, the reader is referred to the web version of this article.)

with an adsorption energy of −0.73 eV, and the resulting equilibrium structure is shown in Fig. 5(i). Since the O adsorption at the T8 site resembles the tetrahedron in bulk Cu_2O and may signal the onset of the Cu_2O formation, we examine the atomic structure of the tetrahedron resulted from the most stable configuration in which the O atom adsorbs to the T8 site, shown in Fig. 5(e). The Cu-O bond lengths range from 1.91 Å to 1.98 Å and Cu-O–Cu bond angles fall between 89.5° and 139.3°. The bond length and bond angle determined from our DFT calculations of bulk Cu_2O are 1.86 Å and 109.47°, respectively. Despite their relative closeness in the bond lengths, the bond angle discrepancy from the perfect Cu_2O tetrahedron suggests that the tetrahedron resulted from the O adsorption at T8 has a distorted tetrahedral structure. We also employ the NEB method to exanimate the energy barrier for an O atom to diffuse to the T8 site to form the tetrahedron. We use the relaxed structure resulting from an O atom adsorbed at the op site (it is the second most stable site with the adsorption energy of −0.52 eV at the oxygen coverage $\theta = 0.69$) as the initial state, and choose the oxygen atom adsorbed at T8 as the final state. Our NEB calculation shows that the energy barrier is 0.51 eV, which is slightly smaller than the barrier (0.53 eV) for the diffusion of atomic oxygen on the (2×1) surface along the [100]

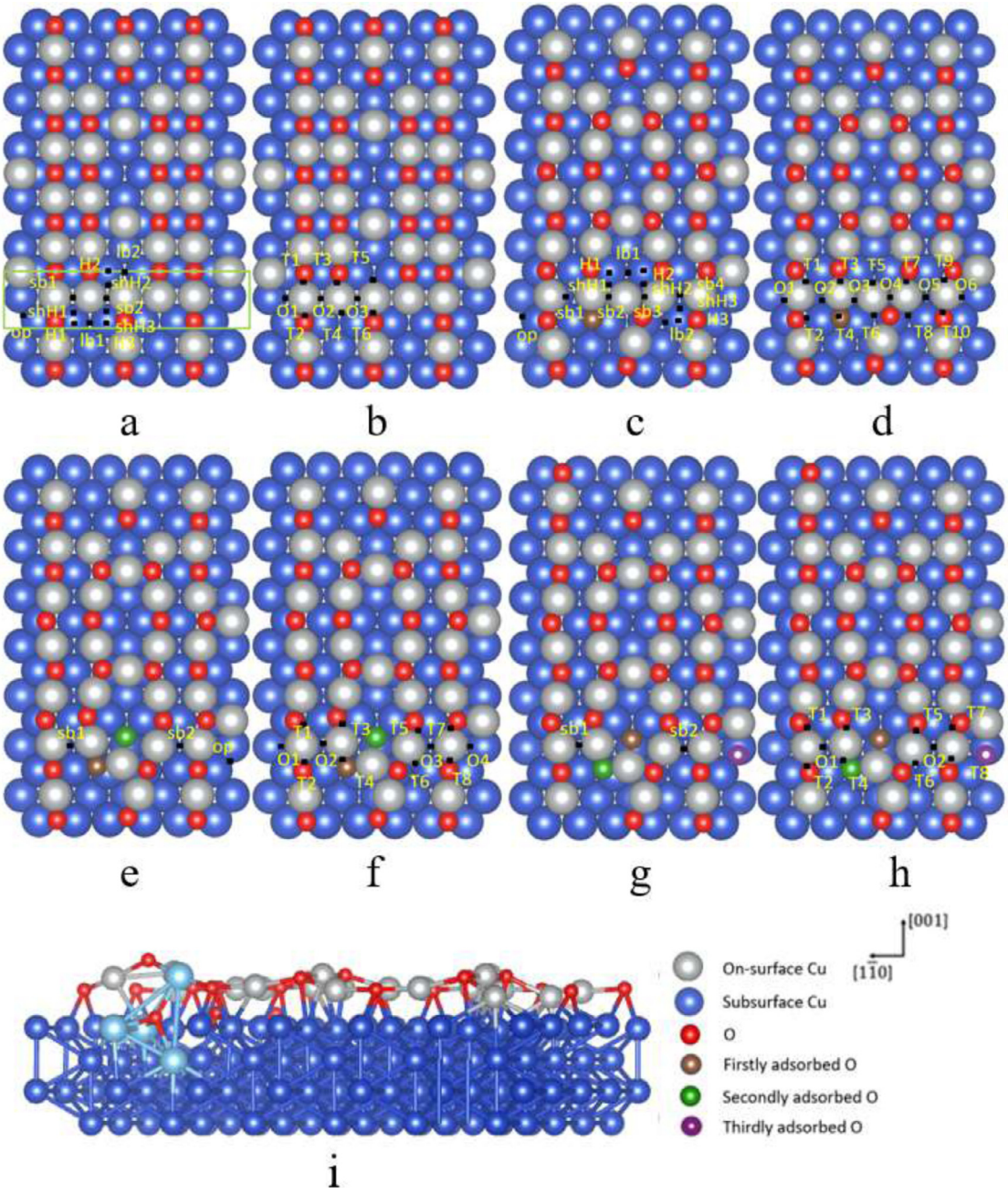

Fig. 6. [1$\bar{1}$0]-IV boundary and the approximate locations of adsorption sites for possible (a) on-surface adsorption sites at coverage $\theta = 0.59$, (b) subsurface adsorption sites $\theta = 0.59$. (c) on-surface adsorption sites at coverage $\theta = 0.61$, (d) subsurface adsorption sites $\theta = 0.61$. (e) on-surface adsorption sites at coverage $\theta = 0.64$, (f) subsurface adsorption sites $\theta = 0.64$. (g) on-surface adsorption sites at coverage $\theta = 0.67$, (h) subsurface adsorption sites $\theta = 0.67$. (i) The equilibrium structure of the tetrahedron formed from the oxygen subsurface adsorption at T6 at the oxygen coverage $\theta = 0.69$ and the resulting Cu_2O-like tetrahedron is highlighted in blue. Similarly, the green rectangle represents the oxygen adsorption area at [1$\bar{1}$0]-type boundaries. (For interpretation of the references to colour in this figure legend, the reader is referred to the web version of this article.)

direction in between the Cu–O–Cu–O chains to supply extra O atoms for the $(2\times1)\rightarrow(6\times2)$ phase transition (if extra Cu is available as well). These NEB calculations indicate that the penetration of the on-surface O atom to the subsurface tetrahedral site is both thermodynamically and kinetically favorable than the on-surface O adsorption for the growth of the (6×2) phase along the $(2\times1)/(6\times2)$ boundary.

The possible adsorption locations for oxygen occupancy along the [1$\bar{1}$0]-IV boundary are identified and marked in Fig. 6. The calculated O binding energy for each site is listed in Table 5. We then add another O atom into the [1$\bar{1}$0]-IV boundary of the most stable configuration with the oxygen occupancy at the lb1 site and achieve a higher oxygen coverage of $\theta = 0.64$. All the nonequivalent on-surface and subsurface sites for possible O occupancy are identified and marked in Fig. 6(c and d), respectively. At this time, oxygen placed at either O4 or T5 site can yield the lowest system energy (adsorption energy −1.32 eV), but oxygen atom cannot stabilize at these sites. The relaxed structure shows that the O atom initially placed at the O4 or T5 site diffuses outward and stabilizes at a new open site formed by the displacement of on-surface Cu and O atoms, i.e., the on-surface Cu atom in the middle of the boundary is pushed to the (2×1) area and moves upward by ~ 0.63 Å; the O atom at the lb site is pushed along the [1$\bar{1}$0] direction. We then add the third oxygen atom into the [1$\bar{1}$0]-IV boundary of the most stable configuration with the oxygen occupancy at the lb1 and the new open site to reach the higher oxygen coverage of $\theta = 0.67$. All the possible on-

Table 5
Oxygen adsorption energies for all the possible sites along the [1$\bar{1}$0]-IV boundary at the oxygen coverage $\theta = 0.59$, 0.61, 0.64, and 0.67, respectively.

	$\theta = 0.59$		$\theta = 0.61$		$\theta = 0.64$		$\theta = 0.67$	
	E_{ads}(eV)	Stabilize site	E_{ads}(eV)	Stabilize site	E_{ads}(eV)	Stabilize site	E_{ads}(eV)	Stabilize site
lb1	−1.90		−1.05					
lb2	−1.24		−0.69					
sb1	−1.90	lb1	−0.63	O2	−0.47	O2	−0.41	O1
sb2	−0.84	O1	−0.99	O3	−0.60	O3	−0.41	O2
sb3			−1.11	shH2				
sb4			−0.70	O5				
H1	−1.89	lb1	−1.11	shH1				
H2	−1.24	Lb2	−1.05	lb1				
H3	−1.89	lb1	−0.67					
shH1	−1.17		−1.05	lb1				
shH2	−1.90	lb1	−1.11					
shH3	−1.12		−0.70					
op	−1.05		−0.83		−0.82			
O1	−0.69		−0.53		−0.56		−0.41	
O2	−0.90		−0.63		−0.47		−0.41	
O3	−1.04		−0.99		−0.60			
O4			−1.32	open	−0.65			
O5			−0.70					
O6			−0.68					
T1	−0.53		−0.65		−0.47	O2	−0.52	
T2	−0.90	O2	−0.63	O2	−0.45		−0.41	O1
T3	−0.12		−0.63	O2	−0.47	O2	−0.41	O1
T4	−1.90	lb1	−0.63	O2	−0.38		−0.35	
T5	−1.24	lb2	−1.32	open	−0.60	O3	−0.41	O2
T6	−0.32		−0.40		−0.78		−0.63	
T7			−0.70	O5	−0.54		−0.52	
T8			−0.56		−0.60	O3	−0.41	O2
T9			−0.57					
T10			−0.68	O6				

surface and subsurface sites for O occupancy are identified and marked in Fig. 6(e and f). The most favorable site for the third O adsorption is the on-surface op site with the O binding energy of −0.82 eV By adding the forth O atom into the [1$\bar{1}$0]-IV boundary of the most stable configuration with the resulting oxygen occupancy at lb1, open and op sites, we reach the oxygen coverage of $\theta = 0.69$. All the possible on-surface and subsurface sites for O adsorption are marked in Fig. 6(g and h). At this oxygen coverage, the tetrahedral site T6 yields the lowest adsorption energy −0.63 eV. The equilibrium structure of the tetrahedron resulted from the O adsorption at T6 is shown in Fig. 6(i) and the measured bond lengths of the tetrahedron ranges from 1.92 Å to 2.04 Å, and the Cu-O–Cu bond angles fall between 86° and 135°, suggesting that it is a distorted tetrahedron compared with that in bulk Cu_2O. Similarly, we used the NEB method to calculate the energy barrier for the diffusion of an on-surface O atom to this subsurface site. We choose the nearest on-surface site sb2 as the initial site and the subsurface site T6 as the finale site. Our NEB calculations show that the kinetic barrier is only 0.16 eV. Such a small barrier suggests that the oxygen subsurface adsorption at the T6 site is both thermodynamically and kinetically favorable than on-surface O adsorption for the growth of the (6 × 2) phase.

3.2. [100]-type boundaries

We then continue the investigation by adsorbing O to the [100]-type boundaries. Fig. 7 shows all the possible on-surface and subsurface adsorption sites in, which contains 171 Cu atoms and 24 O atoms ($\theta = 0.67$). We notice that the [100]-I boundary area is densely packed with three Cu-O adatom rows, which may result in large surface tension at this area [17,20]. This is because Cu-O rows are only very weakly repulsive when separated by more than one lattice unit, while in our supercell, three Cu-O rows are brought together without any separation. Our DFT calculation shows that this boundary is not stable after adsorbing one O atom. Our results (Table 6) shows that the system energy (−1.06 eV) is significant lower than other surface and subsurface sites when oxygen is placed at subsurface sites T1, T2 and on-surface site sb2. However, the adsorbed O atom placed at these sites cannot stabilize at their original positions; instead it diffuses to the shH site nearby, together with the lateral displacement of the Cu-O–Cu chain at the boundary to the (2 × 1) region by one atomic distance along the [1$\bar{1}$0] direction (Fig. 7(a and c)) to release the surface tension. These results show that the oxygen adsorption at this boundary leads to the shrinkage of the (2 × 1) region while expanding the (6 × 2) area, indicating that the [100]-I boundary facilitates the (2 × 1)→(6 × 2) phase transition if additional Cu atoms are available.

Table 6
Oxygen adsorption energies for distinct on-surface and subsurface sites along the [100]-I boundary at the oxygen coverage $\theta = 0.67$.

site	E_{ads}(eV)	Stabilized site
sb	−1.06	shH, boundary moves toward (2 × 1) reconstruction area
shH	−0.90	
H	−0.93	
O1	−0.90	shH
O2	−0.30	
T1	−1.06	shH, boundary moves toward (2 × 1) reconstruction area
T2	−1.06	shH, boundary moves toward (2 × 1) reconstruction area
T3	−0.24	
T4	−0.37	

Like the [1$\bar{1}$0]-III and [1$\bar{1}$0]-VI boundaries, [100]-II and [100]-III boundaries can be also combined into a supercell, as shown in Figs. 8 and 9. Our calculation shows that the most favorable site for the adsorption of one O atom (reaching the oxygen coverage of $\theta = 0.61$) is the shH1 site for the [100]-II boundary (Fig. 8(a) with adsorption energy −1.37 eV (Table 7,) and shH2 for the [100]-III boundary (Fig. 9(a) with the adsorption energy of −1.07 eV (Table 8). H sites in both boundary [100]-II and -III are not stable for O adsorption, and O atoms will diffuse to shH sites which result in the most negative binding energy, after supercell optimized. The next most stable site for oxygen adsorption along the [100]-II boundary is the shH site with the adsorption energy of −1.19 eV, which is ~ 0.18 eV lower than that of the subsurface site

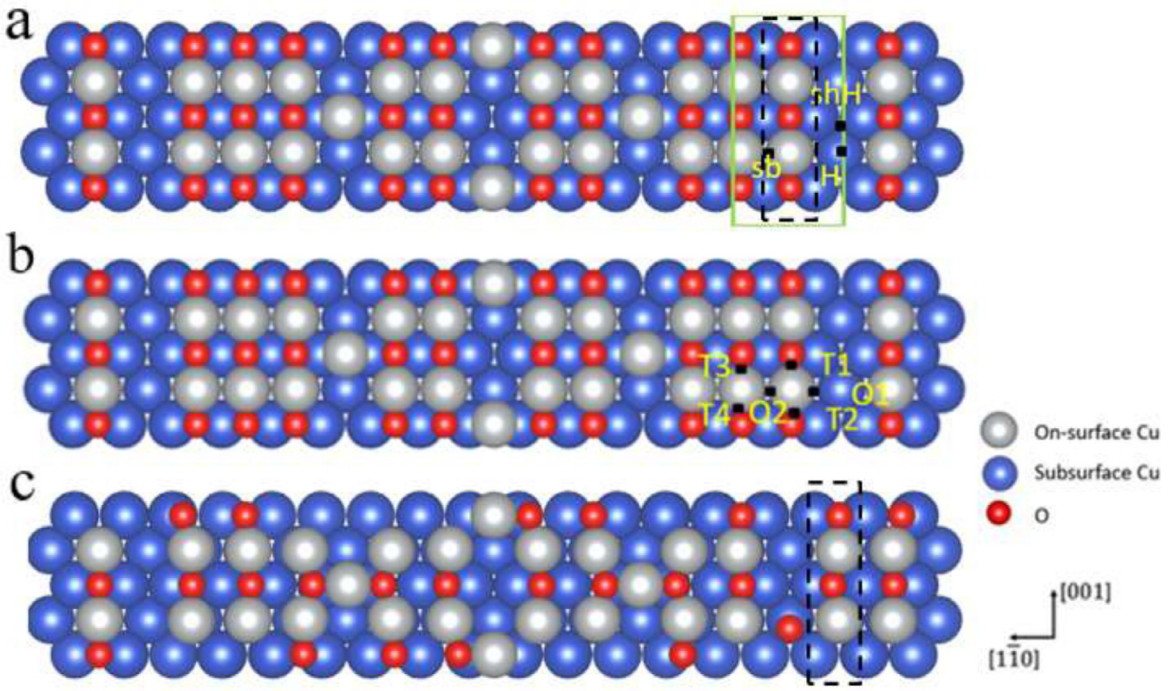

Fig. 7. [100]-I boundary and the approximate locations of adsorption sites for possible (a) on-surface adsorption sites at the initial oxygen coverage $\theta = 0.67$, and (b) subsurface adsorption sites $\theta = 0.67$. (c) The equilibrium structure for oxygen adsorption at T1 or sb. The Cu-O–Cu chain marked by black rectangle shown in (a) and (c) illustrates such chain will diffuse toward (2×1) area with oxygen coverage increasing. The green rectangle shown in (a) represents the boundary area which is within one atomic displacement in the [1$\bar{1}$0] direction perpendicular to the [100]-type boundary. (For interpretation of the references to colour in this figure legend, the reader is referred to the web version of this article.)

Table 7
Oxygen adsorption energies for distinct on-surface and subsurface sites along the [100]-II boundary at the oxygen coverage $\theta = 0.61$, 0.64, and 0.67, respectively. The op1 site at the coverage $\theta = 0.61$ and shH1 site at the coverage $\theta = 0.64$ are marked as op and shH respectively, in Figs. (a, c).

	$\theta = 0.61$		$\theta = 0.64$		$\theta = 0.67$	
	E_{ads}(eV)	Stabilized site	E_{ads}(eV)	Stabilized site	E_{ads}(eV)	Stabilized site
H	−1.37	shH2	−1.19	H to shH1		
shH1	−1.17		−1.19			
shH2	−1.37					
op1	−0.93		−0.88		−0.71	
op2			−0.84		−0.77	
O1	−1.11		−0.55		−0.67	
O2	−0.49		−1.01		−0.41	
O3			−0.88	O3 to op1		
T1	−1.11	O1	−0.38		−0.60	
T2	−0.96		−0.55		−0.60	T2 to T1
T3			−1.01		−0.88	T3 to T4
T4			−0.98		−0.88	

O2. The oxygen occupancy at the shH1 and shH sites reaches the oxygen coverage $\theta = 0.67$ and makes the subsurface tetrahedral site T4 as the most favorable sites for the adsorption of the third O atom (i.e., reaching the oxygen coverage $\theta = 0.69$) with adsorption energy −0.88 eV. The next two most stable sites now are the two op2 sites (Fig. 8(a)) with the adsorption energies of −0.71 eV and −0.77 eV, respectively. Our NEB calculations show that the energy barrier for the oxygen atom diffusing from the on-surface site op2 to the subsurface site T4 is only 0.42 eV, smaller than that for the on-surface diffusion along the [110] channels in the (2×1) region, suggesting that the oxygen occupancy at the subsurface T4 site is both thermodynamically and kinetically favorable. Fig. 8(g) shows the equilibrium structure of the resulting tetrahedron for O adsorption at T4, which has the Cu-O bond lengths ranging from 1.84 Å to 1.96 Å and the Cu-O–Cu bond angles from 97.1° to 128.3°, indicating that it is a distorted tetrahedron compared with the perfect Cu_2O tetrahedron.

Fig. 9(c and d) shows the [100]-III boundary of the most stable configuration with the oxygen occupancy at shH2 and the possible on-surface and subsurface sites for the adsorption of the second O atom along the boundary. The most favorable site for O adsorption is the 5-fold octahedral site O1 with adsorption energy −1.00 eV Noticing that the O adsorption at the O1 site results in the displacement of the previously adsorbed O at the shH2 site due to the O–O repulsive force. The next most favorable site for O adsorption is the subsurface T7 site with the adsorption energy of −0.49 eV (the other tetrahedral sites are not stable for O occupancy). We then add another oxygen atom into the [100]-III boundary of the most stable configuration with the oxygen occupancy at shH2 and O1 and thus reach the oxygen coverage $\theta = 0.69$. Fig. 9(e and f) show the on-surface and subsurface sites, respectively, for possible O adsorption. There are only two on-surface sites, i.e., sb1 and sb2, and O placed initially at these two sites stabilizes at the octahedral sites nearby. While the subsurface T5 site gives the most negative

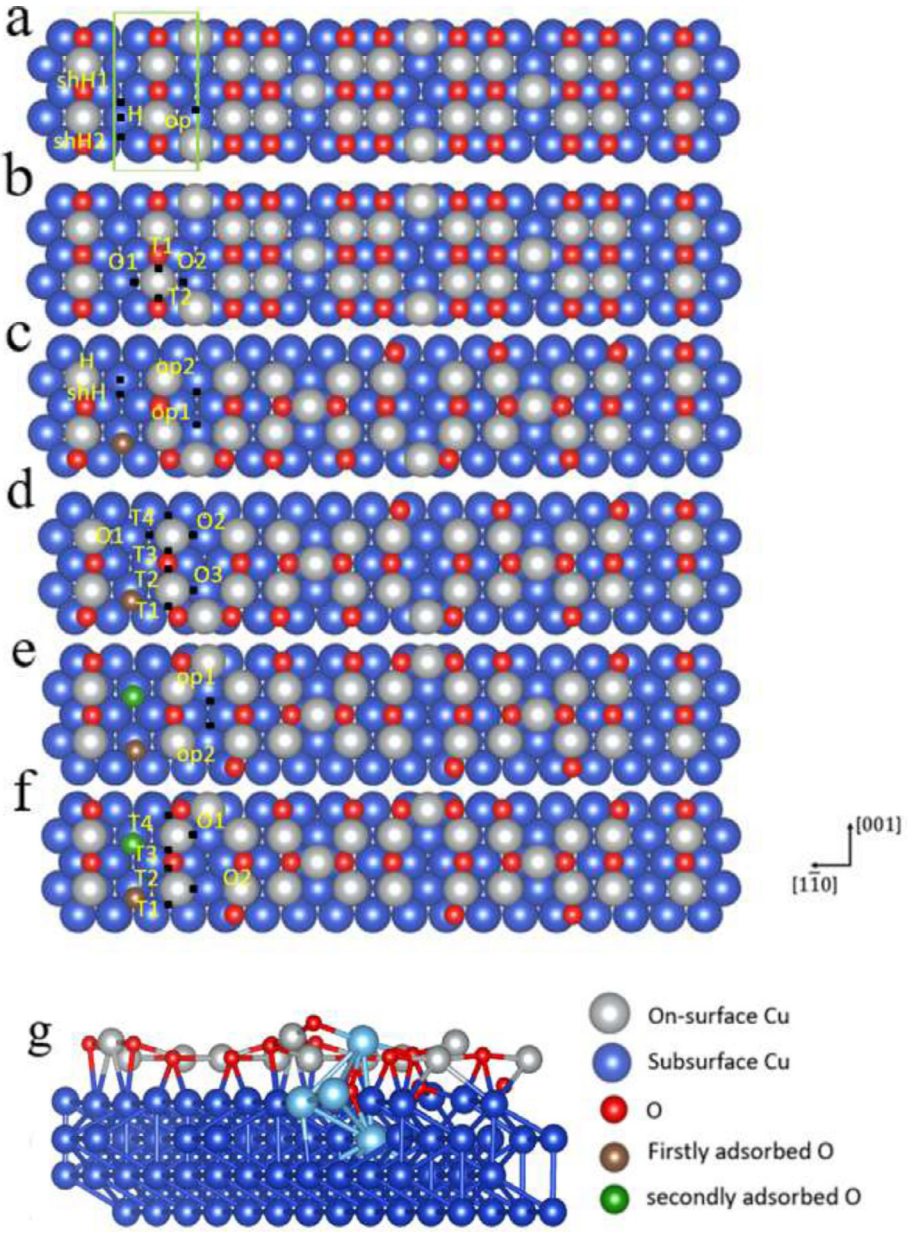

Fig. 8. [100]-II boundary and the approximate locations of adsorption sites for possible (a) on-surface adsorption sites at coverage $\theta = 0.61$, (b) subsurface adsorption sites $\theta = 0.61$. (c) on-surface adsorption sites at coverage $\theta = 0.64$, (d) subsurface adsorption sites $\theta = 0.64$. (e) on-surface adsorption sites at coverage $\theta = 0.67$, (f) subsurface adsorption sites $\theta = 0.67$. (g) The equilibrium structure of the tetrahedron formed from the oxygen subsurface adsorption at T4 for the oxygen coverage $\theta = 0.69$ and the resulting Cu_2O-like tetrahedron is highlighted in blue. Similarly, the green rectangle represents the oxygen adsorption area at the [100] domain boundary. (For interpretation of the references to colour in this figure legend, the reader is referred to the web version of this article.)

adsorption energy, the O atom placed at this site diffuses deeper, stabilizing at the octahedral site between the second and third atomic layers.

Fig. 10(a and b) show all the on-surface and subsurface sites for possible O adsorption along the [100]-IV boundary to reach the oxygen coverage $\theta = 0.64$. Our calculated O adsorption energy of each site is listed in Table 9. There are no short-bridge sites within one atomic displacement of the boundary, and the op site is the most favorable site for O occupancy with the oxygen adsorption energy of −0.96 eV. Oxygen initially placed at T1 also stabilizes at the op site, the subsurface tetrahedral site T2 is the second most favorable site for O occupancy with the adsorption energy of −0.81 eV, which is significant lower than other subsurface sites. We than add another O atom into the [100]-IV boundary of the most stable configuration with the oxygen occupancy at the lb site and achieve a higher oxygen coverage of $\theta = 0.67$. Fig. 10(c and d) show all the possible sites for on-surface and subsurface oxygen adsorption. At this oxygen coverage, on-surface oxygen adsorption no longer yields the lowest energy. There is only one stable on-surface site (op) at the boundary with the oxygen adsorption energy −0.47 eV Although the T3 site yields the lowest adsorption energy, the repulse force from the neighboring oxygen atom pushes the O atom placed at T3 one atomic displacement away from the boundary to shH sites of the (2×1) region. The next most stable adsorption site is the T4 site, which results in the oxygen adsorption energy of −0.85 eV. We also performed NEB calculations to explore the energy barrier for the oxygen atom diffusing from the on-surface op site to the tetrahedral site T4. While the energy barrier of −0.76 eV determined from the NEB calculations is larger than the barrier (~ 0.55 eV) for the on-surface diffusion of O atoms through the channels between Cu-O–Cu chains, it is still lower than the energy barrier of 1.41 eV for the concerted movement of Cu atoms involved in the $(2 \times 1) \rightarrow (6 \times 2)$ phase transition [35]. Thus, it is still possible for

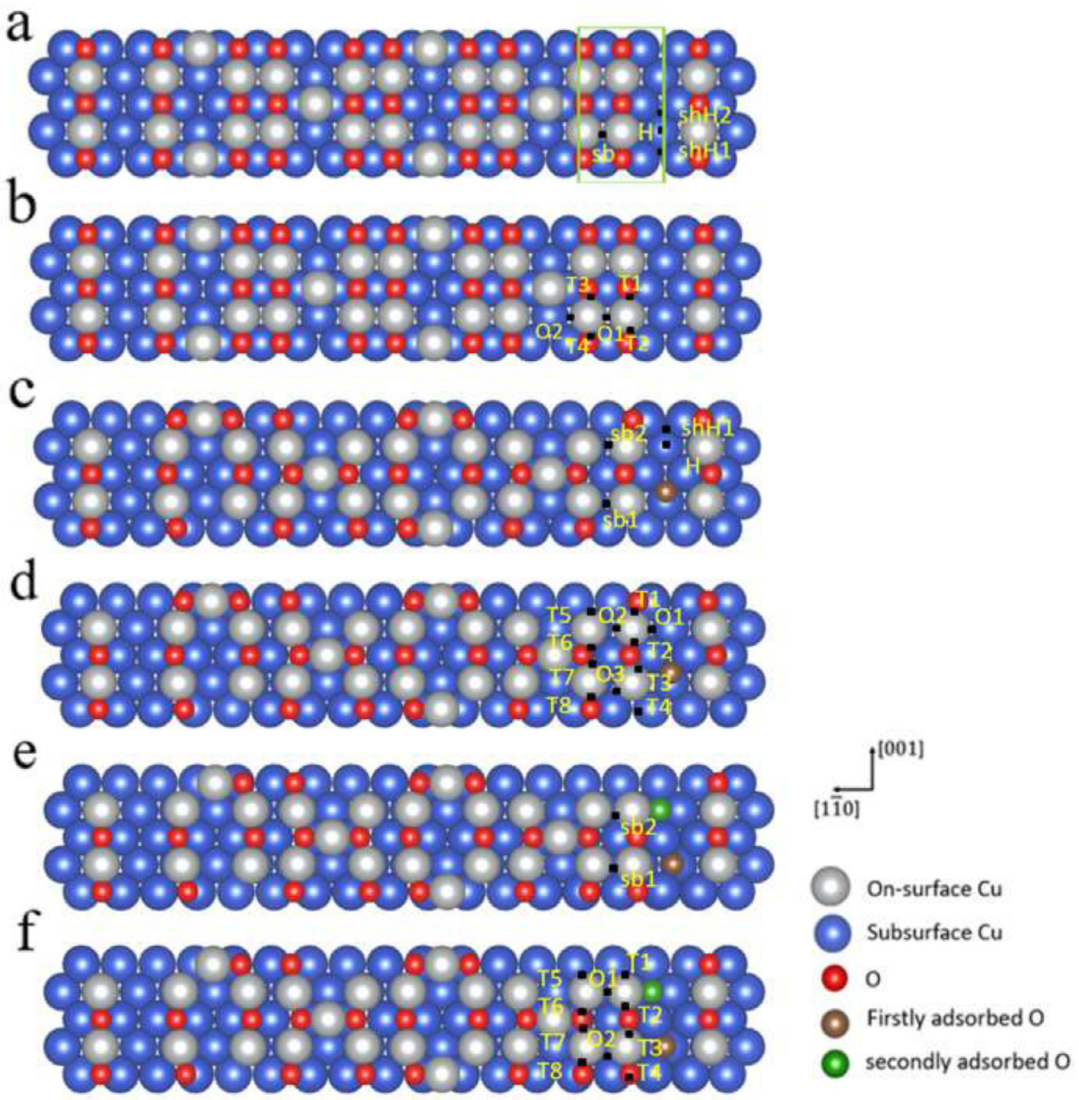

Fig. 9. [100]-III boundary and the approximate locations of adsorption sites for possible (a) on-surface adsorption sites at coverage $\theta = 0.61$, (b) subsurface adsorption sites $\theta = 0.61$. (c) on-surface adsorption sites at coverage $\theta = 0.64$, (d) subsurface adsorption sites $\theta = 0.64$. (e) on-surface adsorption sites at coverage $\theta = 0.67$, (f) subsurface adsorption sites $\theta = 0.67$. Similarly, the green rectangle represents the oxygen adsorption area at the [100] domain boundary. (For interpretation of the references to colour in this figure legend, the reader is referred to the web version of this article.)

Table 8
Adsorption energies for distinct on-surface and subsurface sites at the [100]-III boundary at the oxygen coverage $\theta = 0.61$, 0.64 and 0.67, respectively. The op1 and sb1 sites at coverage $\theta = 0.61$ and the shH1 site at coverage $\theta = 0.64$ is marked as op, sb and shH, respectively, in Figs. 9(a, c).

	$\theta = 0.61$		$\theta = 0.64$		$\theta = 0.67$	
	E_{ads}(eV)	Stabilized site	E_{ads}(eV)	Stabilized site	E_{ads}(eV)	Stabilized site
H	−1.04	shH2	−0.80	H to shH1		
shH1	−0.96		−0.80			
shH2	−1.04					
sb1	−0.96	shH1	−0.35	sb1 to O3	−0.350	sb1 to O2
sb2			−0.27	sb2 to O2	−0.192	sb2 to O1
O1	−0.96	shH1	−1.00		−0.192	
O2	−0.48		−0.27		−0.350	
O3			−0.35			
T1	−0.48	O2	−1.00	T1 to O1	−0.31	
T2	−0.48	O2	−0.48		−0.46	
T3	−0.48	O2	−0.35	T3 to O3	−0.33	
T4	−0.58		−0.35	T4 to O3	−0.17	
T5			−0.27	T5 to O2	−0.72	lower octahedral site
T6			−0.48		0.031	
T7			−0.48		0.14	
T8	–		−0.35	T8 to O3	0.19	

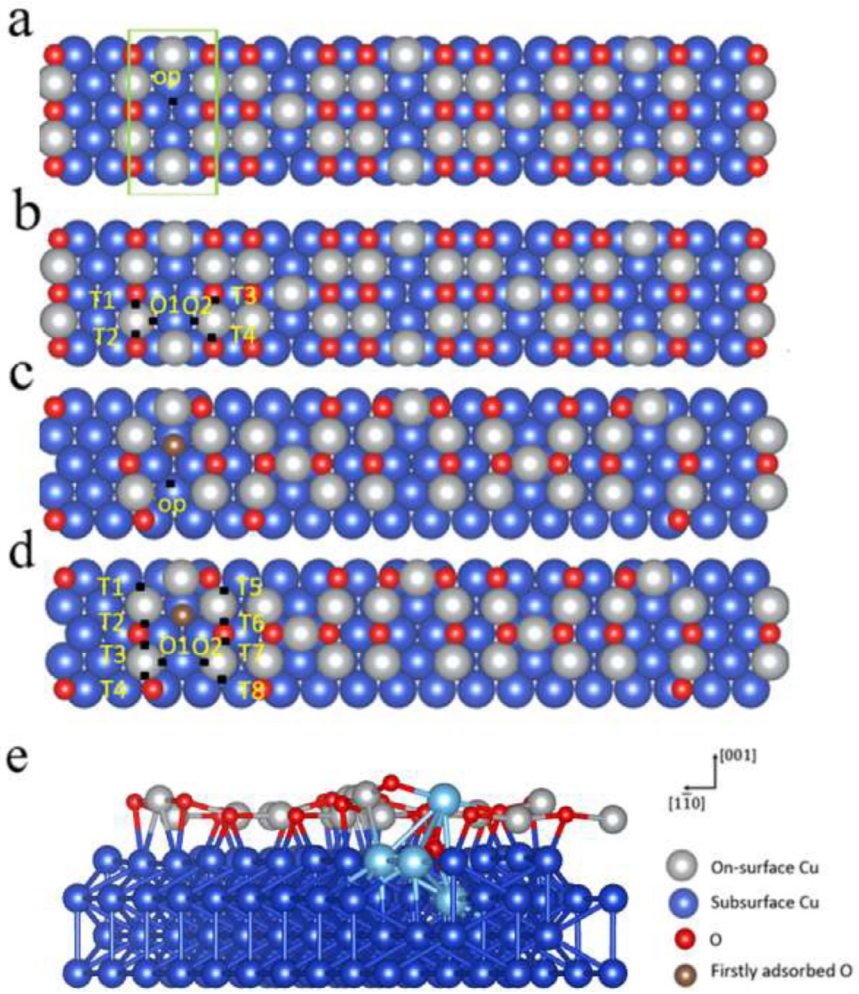

Fig. 10. [100]-IV boundary and the approximate locations of adsorption sites for possible (a) on-surface adsorption sites at coverage $\theta = 0.61$ (b) subsurface adsorption sites $\theta = 0.61$. (c) on-surface adsorption sites at coverage $\theta = 0.64$ (d) subsurface adsorption sites $\theta = 0.64$. (e) The equilibrium structure of the tetrahedron formed from the oxygen subsurface adsorption at T1 for the oxygen coverage $\theta = 0.67$ and the resulting Cu_2O-like tetrahedron is highlighted in blue. The green rectangle represents the oxygen adsorption area at the [100] domain boundary. (For interpretation of the references to colour in this figure legend, the reader is referred to the web version of this article.)

Table 9
Oxygen adsorption energies for distinct on-surface and subsurface sites along the [100]-IV boundary at the oxygen coverage $\theta = 0.64$ and $\theta = 0.67$.

site	$\theta = 0.64$		$\theta = 0.67$	
	E_{ads}(eV)	Stabilized site	E_{ads}(eV)	Stabilized site
op	−0.96		−0.47	
O1	−0.49		−0.40	
O2	−0.57		−0.56	
T1	−0.96	op	−0.55	
T2	−0.81		−0.42	
T3	−0.57		−1.02	move away from the boundary
T4	−0.56	O2	−0.85	
T5			−0.32	
T6			−0.56	O2
T7			−0.60	
T8			−0.59	

Table 10
Oxygen adsorption energies for distinct on-surface and subsurface sites at the [100]-V boundary at the oxygen coverage $\theta = 0.67$.

site	E_{ads}(eV)	Stabilized site
op	−0.74	
sb	−0.49	O1
O1	−0.49	
O2	−0.50	
T1	−0.49	O1
T2	−0.49	O1
T3	−0.49	O1
T4	−0.59	

oxygen diffusing to the subsurface and embedding itself at the tetrahedral T4 site. Once again, the tetrahedron resulted from the O adsorption at the T4 site is a distorted tetrahedron with the bond lengths ranging from 1.86 Å to 2.03 Å and the Cu-O–Cu bond angles between 87.6° and 124.8° as measured from the equilibrium structure of the tetrahedron shown in Fig 10(e).

Figs. 11 and 12 show the approximate locations of adsorption sites for possible on-surface and subsurface oxygen adsorption along the [100]-V and [100]-VI boundaries and the calculated oxygen adsorption energies for the different sites are listed in Tables 10 and 11. Although the initial oxygen coverage is relatively large (after adding one oxygen atom, the surface coverage reaches $\theta = 0.69$) for both boundaries, none of them yields tetrahedral occupancy with the adsorption of an additional O atom. The most favorable site for O adsorption along the [100]-V boundary is the on-surface op site with the adsorption energy of −0.74 eV, and the subsurface T4 site is the next favorable site with the oxygen adsorption energy of −0.59 eV Boundary [100]-VI is very similar

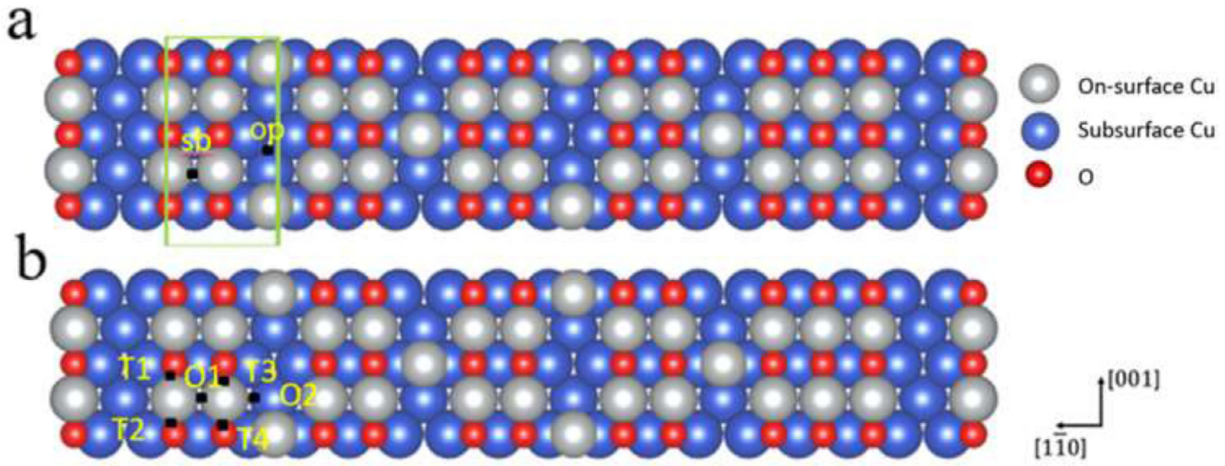

Fig. 11. [100]-V boundary and the approximate locations of adsorption sites for possible (a) on-surface adsorption sites at coverage $\theta = 0.67$, (b) subsurface adsorption sites $\theta = 0.67$. The green rectangle represents the oxygen adsorption area at the [100] domain boundary. (For interpretation of the references to colour in this figure legend, the reader is referred to the web version of this article.)

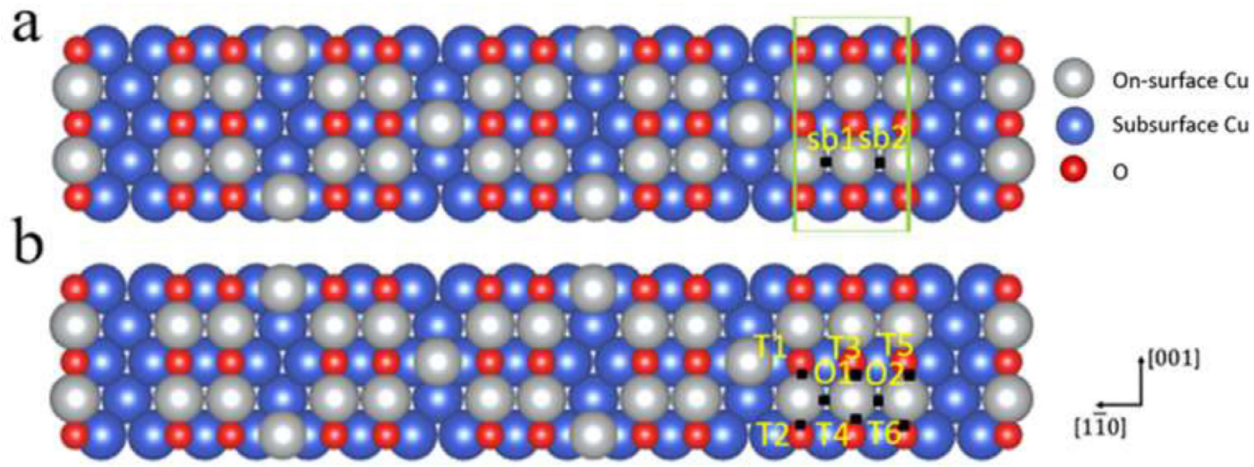

Fig. 12. [100]-VI boundary and the approximate locations of adsorption sites for possible (a) on-surface adsorption sites at coverage $\theta = 0.67$, (b) subsurface adsorption sites $\theta = 0.67$. Similarly, the green rectangle represents the oxygen adsorption area at the [100] domain boundary. (For interpretation of the references to colour in this figure legend, the reader is referred to the web version of this article.)

Table 11
Oxygen adsorption energies for distinct on-surface and subsurface sites along the [100]-VI boundary at the oxygen coverage $\theta = 0.67$.

Site	E_{ads}(eV)	Stabilized site
sb1	−0.38	O1
sb2	−0.29	O2
O1	−0.38	
O2	−0.29	
T1	−0.52	
T2	−0.24	
T3	−1.04	shH, boundary moves toward (2×1) reconstruction area
T4	−0.38	O1
T5	−0.29	O2
T6	−1.04	shH, boundary moves toward (2×1) reconstruction area

to boundary [100]-I, consisting three Cu-O–Cu chains in the boundary area. Oxygen placed at T3 and T6 can yield the lowest system energy, but one Cu-O–Cu chain within the boundary diffuses toward the (2×1) region, leading to the expansion of the (6×2) region. Thus, both the [100]-V and -VI boundaries have the tendency to propagate along with the (2×1)→(6×2) phase transition rather than promoting subsurface O adsorption.

By examining the oxygen adsorption along the different heterophase boundaries shown above, we can find that the oxygen atoms tend to stabilize at the subsurface site as oxygen coverage increases. With increasing oxygen coverage, the strong repulse force between the on-surface oxygen atoms results in a sharp decrease of the heat of adsorption, and enables oxygen subsurface site occupation. Such a tendency is also noticed from the oxygen adsorption at the perfectly reconstructed surfaces such as the Cu(100)-$(2\sqrt{2}\times\sqrt{2})R45°$-O and Cu(110)-(6×2)-O [28,49]. For oxygen adsorption at the perfectly reconstructed Cu(110)-(6×2)-O surface, a critical oxygen coverage of $\theta = 1$ is required to form the Cu_2O-like tetrahedrons in the subsurface region [28]. The (2×1)→(6×2) phase transition on the Cu (110) results in the formation of different boundaries. Our DFT results show that the oxygen adsorption at the boundaries of [1$\bar{1}$0]-I, -II, and [100]-I, -III, -V, -VI conduces the (2×1)→(6×2) phase transition while the boundaries of [1$\bar{1}$0]-III, -IV and [100]-II, -IV aid subsurface oxygen adsorption to form Cu_2O-like tetrahedrons at the oxygen coverage $\theta < 0.69$ thereby facilitating the onset of the internal oxidation.

By comparing the oxygen adsorption along the different (2×1)/(6×2) boundaries, we can find that the Cu_2O-like tetrahedron tends to nucleate at the boundaries that show a larger surface protrusion. As mentioned above, the average bond length between Cu and O atoms in the resulting tetrahedron is around 1.92 Å, which is smaller than the Cu-O bond length (~ 2.10 Å) in the resulting octahedron. The formation of strong and shorter Cu-O bonds in the tetrahedral site implies a stronger attractive interaction between the sub-surface atoms, which could effectively screen the O–O repulsion

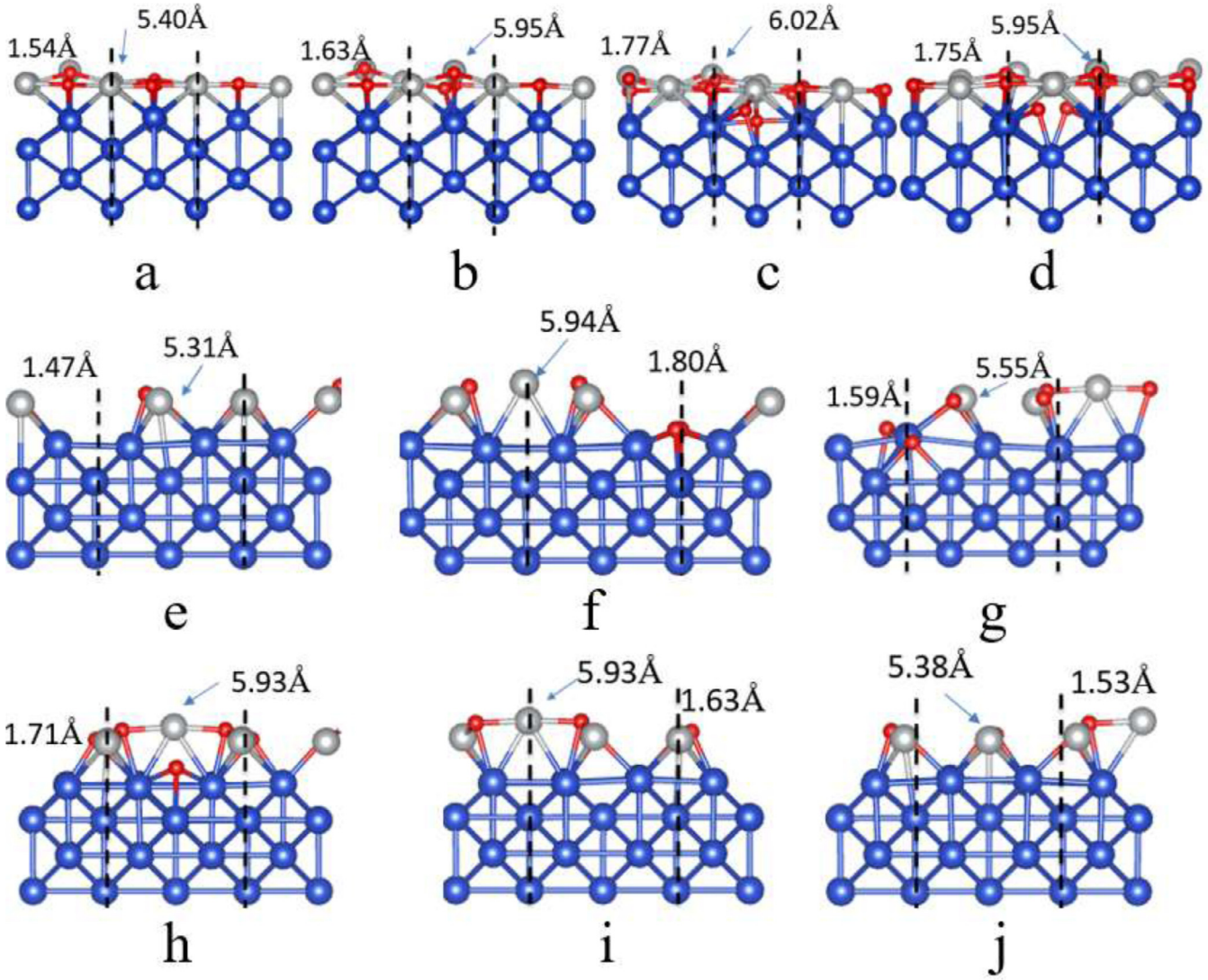

Fig. 13. Side view of the equilibrium structures of all the ten boundaries resulting from the most sable adsorption at the oxygen coverage $\theta = 0.67$ (the oxygen coverage for [100]-IV is $\theta = 0.64$). (a) [1$\bar{1}$0]-I, (b) [1$\bar{1}$0]-II, (c) [1$\bar{1}$0]-III, (d) [1$\bar{1}$0]-IV, (e) [100]-I, (f) [100]-II, (g) [100]-III, (h) [100]-IV, (i) [100]-V, (j) [100]-VI. The height of the most protruding Cu atom within the boundary area is given with respect to the bottom of the slab and the interplanar spacing between first and second layers is measured by averaging the surface heights of the Cu atoms in the first and second layer within the boundary area. The boundary area is within one atomic displacement perpendicular to the $(2\times1)/(6\times2)$ boundary and marked by the dotted lines.

as the oxygen coverage increasing. It also should be noted that the oxygen residing at an octahedral site is usually more favorable than at the tetrahedral site. In FCC Cu, the radius of tetrahedral hole is $R_t = 0.225R_{Cu}$, which is much smaller than that of the octahedral hole, $R_o = 0.414R_{Cu}$ (R_{Cu} is the radius of a Cu atom), thus the larger space by the octahedral site can avoid the strain in the lattice to reduce the system energy [29–32]. Previous study has shown that the oxygen surface adsorption can weaken the bonding between the Cu atoms in the first and second layer and induces the upward relaxation of the surface layer [28–31]. The upward relaxation of the topmost layer results in a larger interplanar spacing between the first and second layers and therefore makes room available for oxygen tetrahedral occupancy as the oxygen coverage increases. Fig. 13 shows the equilibrium structures of all the ten boundaries resulting from the most sable oxygen adsorption configuration at the oxygen coverage $\theta = 0.67$, beyond which the adsorption of an additional oxygen atom results in the formation of the Cu_2O-like tetrahedron, i.e., at the oxygen coverage $\theta = 0.69$ (the oxygen coverage for [100]-IV is $\theta = 0.64$, because the critical oxygen coverage for the formation of the Cu_2O-like tetrahedron at [100]-IV is $\theta = 0.67$). As shown in Fig. 13, the interplanar spacing between the first and second layers of the boundaries of [1$\bar{1}$0]-I, and [100]-I, -III -VI is much smaller than that of the other boundaries, therefore the tetrahedral sites associated with these four boundaries are less favorable for oxygen occupancy. By contrast, the larger surface elevation of the Cu atoms (a surface elevation of ~ 0.63 Å compared with the perfect (2×1)) in the boundary area associated with the [1$\bar{1}$0]-III, -IV and [100]-II, -IV boundaries results in a larger interplanar spacing between the top and second layers of the Cu atoms, which in turn increases the volume for the tetrahedral sites located between the first and second layers thereby facilitating oxygen uptake by these tetrahedral sites as the oxygen coverage increases. It is worth mentioning that oxygen atoms cannot stabilize at the tetrahedral sites associated with the [1$\bar{1}$0]-II and [100]-V boundaries, although the Cu atoms at these two boundaries also develop a surface protrusion. This is because the interplanar spacings between the first and second layers of the [1$\bar{1}$0]-II and [100]-V boundaries are ~1.63 Å, which are smaller than those for the [1$\bar{1}$0]-III, -IV and [100]-II, -IV boundaries that have the interplanar spacings of 1.77 Å, 1.75 Å, 1.80 Å and 1.71 Å, respectively. The smaller interplanar spacings for the [1$\bar{1}$0]-II and [100]-V boundaries make the additional oxygen tetrahedral occupancy unfavorable for those two boundaries.

4. Conclusion

By using the DFT calculation, we explore the stability and structural change of the heterophase boundaries formed by the $(2\times1)\rightarrow(6\times2)$ phase transformation at the Cu (110) surface. Upon the increased oxygen coverage, we find that some boundaries allow for further propagation of the $(2\times1)/(6\times2)$ phase boundary while the other boundaries promote subsurface oxygen adsorption that results in the formation of Cu_2O-like tetrahedrons. By comparing the surface height of the Cu atoms within the boundary area, we show that the boundaries with a larger surface elevation of the Cu atoms tend to form Cu_2O-like tetrahedrons by subsurface oxygen occupancy. The results provide fundamental insight into understanding the effect of heterophase boundaries in an oxygen chemisorbed overlayer on the subsequent oxygen adsorption on the onset of internal oxidation. While oxygen chemisorption induced surface restructuring is a typical phenomenon for metal-oxygen systems, the effect of defects in an oxygen chemisorbed layer on the onset of bulk oxide formation has hitherto rarely been addressed. The results and approach reported in this work may find broader applicability to other metal-oxygen systems that involve progressive stages of oxygen chemisorption induced surface phase transition and restructuring.

Acknowledgements

This work was supported by the U.S. Department of Energy, Office of Basic Energy Sciences, Division of Materials Sciences and Engineering under Awards No. DE-SC0001135. This research used the computational resources of the Center for Functional Nanomaterials, which is a U.S. DOE Office of Science Facility, at Brookhaven National Laboratory under Contract No. DE-SC0012704. This work used the computational resources from the Extreme Science and Engineering Discovery Environment (XSEDE), which is supported by National Science Foundation grant number OCI-1053575.

Supplementary materials

Supplementary material associated with this article can be found, in the online version, at doi:10.1016/j.susc.2017.08.017.

References

[1] A.O. Musa, T. Akomolafe, M.J. Carter, Sol. Cells 51 (1998) 305–316.
[2] P.J. Sebastian, J. Quintana, F. Avila, X. Mathew, Surf. Eng. 16 (2000) 47–49.
[3] H. Over, Y.D. Kim, A.P. Seitsonen, S. Wendt, E. Lundgren, M. Schmid, P. Varga, A. Morgante, G. Ertl, Science 287 (2000) 1474–1476.
[4] C. Stampfl, M. Veronica Ganduglia-Pirovano, K. Reuter, M. Scheffler, Surf. Sci. 500 (2002) 368–394.
[5] C. Gattinoni, A. Michaelides, Surf. Sci. Rep. 70 (2015) 424–447.
[6] M. Todorova, W.X. Li, M.V. Ganduglia-Pirovano, C. Stampfl, K. Reuter, M. Scheffler, Phys. Rev. Lett. 89 (2002) 096103.
[7] Q. Zhu, L. Zou, G. Zhou, W.A. Saidi, J.C. Yang, Surf. Sci. 652 (2016) 98–113.
[8] C.I. Carlisle, T. Fujimoto, W.S. Sim, D.A. King, Surf. Sci. 470 (2000) 15–31.
[9] W. Brown, R. Kose, D. King, Chem. Rev. 98 (1998) 797–832.
[10] J. Stuckless, C. Wartnaby, N. Al-Sarraf, S.J. Dixon-Warren, M. Kovar, D. King, J. Chem. Phys. 106 (1997) 2012–2030.
[11] A. Guerrero-Ruiz, I. Rodriguez-Ramos, J. Fierro, Appl. Catal. 72 (1991) 119–137.
[12] R.W. Mayer, M. Hävecker, A. Knop-Gericke, R. Schlögl, Catal. Lett. 74 (2001) 115–119.
[13] C. Fukuhara, H. Ohkura, Y. Kamata, Y. Murakami, A. Igarashi, Appl. Catal. A 273 (2004) 125–132.
[14] G. Ertl, Surf. Sci. 6 (1967) 208–232.
[15] R. Feidenhans, I. Stensgaard, Surf. Sci. 133 (1983) 453–468.
[16] D. Coulman, J. Wintterlin, R. Behm, G. Ertl, Phys. Rev. Lett. 64 (1990) 1761.
[17] R. Feidenhans, F. Grey, M. Nielsen, F. Besenbacher, F. Jensen, E. Lægsgaard, I. Stensgaard, K.W. Jacobsen, J.K. Nørskov, R. Johnson, Phys. Rev. Lett. 65 (1990) 2027.
[18] F. Frechard, R. Van Santen, Surf. Sci. 407 (1998) 200–211.
[19] C. Poulain, F. Wiame, V. Maurice, P. Marcus, Surf. Sci. 606 (2012) L26–L30.
[20] X. Duan, O. Warschkow, A. Soon, B. Delley, C. Stampfl, Phys. Rev. B 81 (2010).
[21] X. Lian, P. Xiao, S.-C. Yang, R. Liu, G. Henkelman, J. Chem. Phys. 145 (2016) 044711.
[22] L. Guillemot, K. Bobrov, Phys. Rev. B 83 (2011) 075409.
[23] K. Bobrov, L. Guillemot, Surf. Sci. 604 (2010) 1894–1898.
[24] L. Li, N. Cai, W.A. Saidi, G. Zhou, Chem. Phys. Lett. 613 (2014) 64–69.
[25] S. Liem, G. Kresse, J. Clarke, Surf. Sci. 415 (1998) 194–211.
[26] Q. Liu, L. Li, N. Cai, W.A. Saidi, G. Zhou, Surf. Sci. 627 (2014) 75–84.
[27] L. Li, X. Mi, Y. Shi, G. Zhou, Phys. Rev. Lett. 108 (2012) 176101.
[28] L. Li, G. Zhou, Surf. Sci. 615 (2013) 57–64.
[29] T. Kangas, K. Laasonen, Surf. Sci. 602 (2008) 3239–3245.
[30] T. Kangas, K. Laasonen, A. Puisto, H. Pitkänen, M. Alatalo, Surf. Sci. 584 (2005) 62–69.
[31] M. Lee, A.J. McGaughey, Surf. Sci. 603 (2009) 3404–3409.
[32] M. Lee, A.J. McGaughey, Surf. Sci. 604 (2010) 1425–1431.
[33] J. Wintterlin, J. Vacu. Sci. Technol. B 9 (1991) 902.
[34] F. Besenbacher, Rep. Prog. Phys. 59 (1996) 1737.
[35] L. Li, Q. Liu, J. Li, W.A. Saidi, G. Zhou, J. Phys. Chem. C 118 (2014) 20858–20866.
[36] G. Zhou, L. Luo, L. Li, J. Ciston, E.A. Stach, W.A. Saidi, J.C. Yang, Chemi. Commun. 49 (2013) 10862–10864.
[37] H. Qin, X. Chen, L. Li, P.W. Sutter, G. Zhou, Proc. Natl. Acad. Sci. U.S.A. 112 (2015) E103–E109.
[38] J. Li, L. Li, G. Zhou, J. Chem. Phys. 142 (2015) 084701.
[39] G. Kresse, J. Furthmüller, Phys. Rev. B 54 (1996) 11169.
[40] G. Kresse, J. Hafner, Phys. Rev. B 47 (1993) 558.
[41] G. Kresse, J. Hafner, Phys. Rev. B 49 (1994) 14251.
[42] G. Kresse, J. Furthmüller, Comput. Mater. Sci. 6 (1996) 15–50.
[43] J.P. Perdew, J.A. Chevary, S.H. Vosko, K.A. Jackson, M.R. Pederson, D.J. Singh, C. Fiolhais, Phys. Rev. B 46 (1992) 6671.
[44] G. Kresse, D. Joubert, Phys. Rev. B 59 (1999) 1758.
[45] G. Zhou, L. Luo, L. Li, J. Ciston, E.A. Stach, J.C. Yang, Phys. Rev. Lett. 109 (2012) 235502.
[46] H.J. Monkhorst, J.D. Pack, Phys. Rev. B 13 (1976) 5188.
[47] C. Kittel, D.F. Holcomb, Am. J. Phys. 35 (1967) 547–548.
[48] G. Henkelman, B.P. Uberuaga, H. Jónsson, The J. Chem. Phys. 113 (2000) 9901–9904.
[49] M. Lee, A.J. McGaughey, Phys. Rev. B 83 (2011) 165447.